ChemComm

COMMUNICATION

View Article Online
View Journal | View Issue

Cite this: *Chem. Commun.*, 2021, **57**, 7304

Received 15th April 2021,
Accepted 30th June 2021

DOI: 10.1039/d1cc02014e

rsc.li/chemcomm

Synthesis of high surface area $CaSO_4{\cdot}0.5H_2O$ nanorods using calcium ethoxide as precursor†

Miguel Burgos-Ruiz, Gloria Pelayo-Punzano, Encarnacion Ruiz-Agudo, Kerstin Elert and Carlos Rodriguez-Navarro *

We report a novel solvothermal route for the production of bassanite ($CaSO_4{\cdot}0.5H_2O$) nanoparticles using amorphous Ca-ethoxide as a precursor. Bassanite nanorods, 120–200 nm in length, with the highest specific surface area reported so far (54 $m^2\ g^{-1}$) and enhanced reactivity, are obtained at 78 °C and 1 atm. Such nanoparticles may find application in several fields, including biomaterials, drug delivery, and cultural heritage conservation.

Calcium sulfates are abundant in nature, currently being among the most demanded and massively produced inorganic materials worldwide.[1] They find a broad range of applications in construction,[2] heritage conservation,[3] bone regeneration,[4] dental prosthetics,[5] and drug delivery.[4a,6]

Different solid calcium sulfate phases exist: gypsum ($CaSO_4{\cdot}2H_2O$), bassanite or hemihydrate (α- and β-$CaSO_4{\cdot}0.5H_2O$; note that the existence of two distinct bassanite polymorphs is currently under debate),[1,7] and anhydrite (α-, β- and γ-$CaSO_4$). Among them, hemihydrate is of particular interest due to its high reactivity, excellent biocompatibility, and optimal mechanical properties once hydrated to gypsum:[1–8] set β-hemihydrate (standard plaster of Paris) has a compressive strength <20 MPa, and set α-$CaSO_4{\cdot}0.5H_2O$ (*e.g.*, dental gypsum) can reach compressive strength >40 MPa.[8] Plaster of Paris is produced by heating gypsum at 110–220 °C and 1 atm under dry conditions.[7,8] Multiple energy intensive/complex routes for α-hemihydrate have been proposed, including dehydration of gypsum in electrolyte (acid) solutions, in water (and water/alcohol) or in steam (autoclave),[9] oxidation of calcium sulfite,[10] microwave-assisted synthesis,[11] electrochemical deposition,[12] or reaction of Ca^{2+} and SO_4^{2-} ions in aqueous (or alcohol/water) solutions in the presence/absence of organic additives/surfactants, with and without ultrasonication.[13] All of these routes typically produce micrometer sized bassanite crystals with varying aspect ratios. Recently, efforts have been made to produce more reactive bassanite nanoparticles (length < 100–500 nm) for improved applications. This is, however, challenging.

Interestingly, precipitation in the $CaSO_4$–H_2O system follows a non-classical multi-step sequence involving amorphous calcium sulfate and metastable bassanite precursor nanoparticles prior to stable gypsum,[1,14] which might enable access to intermediate (meta)stable nanophases.[15] Following this approach, Wang and Meldrum stabilized bassanite nanocrystals using different additives,[16] while Cölfen and co-workers obtained hemihydrate nanorods 50–200 nm in size by quenching diluted Na_2SO_4 and $CaCl_2$ solutions in different alcohols.[17] Recently, Chen *et al.*[18] used $CaCl_2$, $(NH_4)_2SO_4$ and Na_2EDTA ethylene glycol–water solutions to obtain ellipsoidal hemihydrate mesocrystals 300–500 nm in length, made up of nanorods with lengths of 30–80 nm and widths of 10–20 nm, which disaggregated upon EDTA removal. However, the precipitation of NaCl or NH_4Cl as by-products or the presence of residual additives in the above-mentioned routes raises the problem of their later elimination, which is typically done by washing cycles using water, thus enabling coarsening by Ostwald ripening. Byproducts-free bassanite nanoparticles with specific surface area (SSA) of up to 33.3 $m^2\ g^{-1}$ (to our knowledge, the highest SSA reported so far) were obtained following freeze drying of a saturated $CaSO_4$ solution and oven-heating of the obtained powder at 150 °C for 30′.[19] However, this synthesis route is energy intensive, and the yield is very small due to the low solubility of $CaSO_4$ (~2 g L^{-1} at 20 °C).

Here we report on a novel, high-yield, one-pot mild route for the synthesis of phase-pure $CaSO_4{\cdot}0.5H_2O$ nanorods with no residual additive or background electrolyte and showing the highest SSA achieved to date. The reaction proceeds according to (for details see Materials and methods in ESI†):

$$Ca^0 + 2C_2H_5OH \rightarrow Ca(OC_2H_5)_2 + H_2\uparrow \quad (1)$$

$$Ca(OC_2H_5)_2 + 2H_2O \rightleftarrows Ca(OH)_2 + 2C_2H_5OH \quad (2)$$

Dept. Mineralogy and Petrology, University of Granada, Fuentenueva s/n, Granada, 18002, Spain. E-mail: carlosrn@ugr.es

† Electronic supplementary information (ESI) available: Details of the experimental protocol, analytical techniques, kinetic model, and supplementary figures. See DOI: 10.1039/d1cc02014e

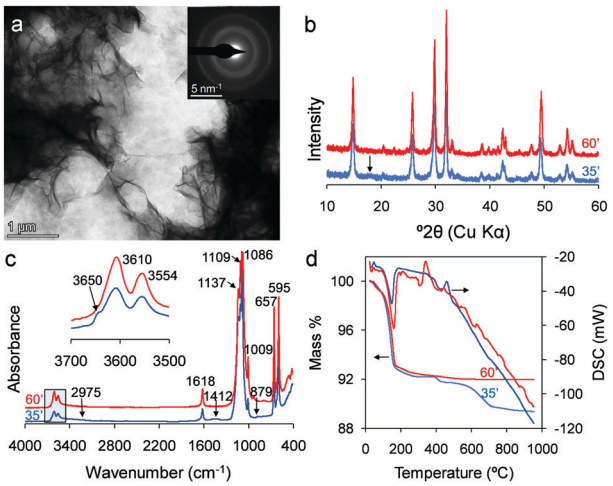

Fig. 1 Characterization of precursor and product phases. (a) TEM image of Ca-ethoxide (flake-like aggregates). The SAED pattern (inset) shows diffuse haloes demonstrating the amorphous nature of this precursor phase; (b) XRD patterns of product obtained at 35′ and 60′. Note the presence, in addition of the intense bassanite peaks, of a small broad peak corresponding to 001 portlandite (arrow) in the sample collected at 35′; (c) FTIR spectra of products obtained at 35′ and 60′. The inset shows a detail of the O–H stretching of crystal water in bassanite and the shoulder at 3650 cm^{-1} of portlandite (after 35′); (d) TG/DSC traces of products obtained after 35′ and 60′ reaction time.

$$Ca(OH)_2 + H_2SO_4 \rightarrow CaSO_4{\cdot}0.5H_2O + 1.5H_2O \quad (3)$$

First, the irreversible redox reaction between metallic calcium and a molar excess of absolute ethanol yields a homogeneous whitish alcoholic suspension of amorphous calcium ethoxide, as shown by transmission electron microscopy (TEM) and selected area electron diffraction (SAED) (Fig. 1a), as well as infrared spectroscopy analysis (FTIR) (Fig. S1, ESI†). Subsequently, bassanite nanoparticles precipitate through a two-step mechanism upon addition of toluene and a H_2SO_4 solution in a 1 : 1 Ca^0 : SO_4^{2-} molar ratio. The toluene- and acid-catalyzed hydrolysis of calcium ethoxide leads to the formation of calcium hydroxide (eqn (2)), which serves as precursor for the precipitation of $CaSO_4{\cdot}0.5H_2O$ nanorods *via* an acid–base neutralization (eqn (3)). Addition of non-polar toluene results in an increase of water activity and hydration rate due to a decrease in the intensity of electrostatic intermolecular forces.[20] In the absence of toluene, the formation of ~1/1 (wt/wt) anhydrite/bassanite mixtures is favored (Fig. S2–S4, ESI†). Modulating both the amount of water and reaction time helps prevent the conversion of bassanite into gypsum, and limits Ostwald ripening phenomena (see below).

X-Ray diffraction (XRD) patterns of powder samples obtained at different reaction times (35, 45, 55 and 60 min) showed that in all cases a monoclinic (space group *I*2) hemihydrate phase was obtained (Fig. 1b). However, at 35′ characteristic Bragg peaks of portlandite were detected, indicating that $Ca(OH)_2$ preceded the precipitation of hemihydrate. Portlandite was no longer observed after ≥45′ reaction time. The crystallite sizes of bassanite determined (for the 200 Bragg peak) using the Scherrer equation ranged from 17 ± 2 nm at 35′ to 25 ± 2 nm at 60′. In contrast, a commercial (control) β-hemihydrate (plaster of Paris) obtained after calcination of gypsum (see Materials and methods in ESI†) showed a crystallite size of 49 ± 2 nm.

FTIR of synthesis products collected at 45′, 55′, and 60′ showed moderate intensity bands at 3554 and 3610 cm^{-1} ascribed to the ν_1 symmetric and ν_3 antisymmetric stretch of water molecules, respectively, along with the δ-OH bending band at 1618 cm^{-1}, indicative of a single type of crystalline water in bassanite (Fig. 1c).[21] The observed moderate intensity ν_1 (SO_4) symmetric stretch band at 1006 cm^{-1} and the ν_3 (SO_4) antisymmetric stretch band at ~1100 cm^{-1}, clearly split into three peaks, are all characteristic of bassanite.[21] The solid sample collected after 35′ showed an additional weak shoulder at 3650 cm^{-1} and a weak and broad doublet at 1412–1485 cm^{-1} (ν_3 asymmetric CO_3 stretch) indicative, respectively, of the existence of trace amounts of $Ca(OH)_2$ and amorphous calcium carbonate (likely formed following the carbonation of $Ca(OH)_2$ upon contact with atmospheric CO_2 during sample handling). Very weak bands at 2975, 2937 and 2884 cm^{-1} corresponding to $-OCH_2CH_3$ groups were also detected in this latter sample. These results show that a small fraction of unreacted Ca-ethoxide and $Ca(OH)_2$ precursors was present after 35′ reaction time.

Simultaneous thermogravimetry and differential scanning calorimetry (TG-DSC) analyses showed that samples collected at 45′, 55′, and 60′ reaction time display a weight loss of ~8 wt% and an endothermic peak at ~160 °C, corresponding to the removal of adsorbed water (1.8 wt%) and crystal water of bassanite (6.2 wt%) (Fig. 1d). In addition, the DSC trace shows a small exothermic peak at ~200 °C, demonstrating the presence of α-hemihydrate.[21] This phase transformed into γ-$CaSO_4$ upon dehydration, which in turn transforms into insoluble anhydrite (β-$CaSO_4$) at such a *T*.[22] However, we also observed an exothermic peak at 345 °C, reportedly corresponding to the transformation γ-$CaSO_4$ → β-$CaSO_4$, after dehydration of β-hemihydrate.[22] This shows that the product is a mixture of α- and β-hemihydrate. No other weight loss was observed, which allowed us to estimate a reaction yield ≥99%. TG-DSC analysis of samples obtained after 35′ showed a weight loss of 1.0 wt% at <100 °C, due to adsorbed water, followed by a marked weight loss of 6.2 wt% ascribed to bassanite dehydration, as well as a single exothermic band at ~190 °C, demonstrating the sole presence of α-hemihydrate (Fig. 1d). In addition, a weight loss of 0.9 wt% at ~400 °C and of 1.9 wt% at ~600 °C, assigned to the dehydroxylation of calcium hydroxide ($Ca(OH)_2 \rightarrow CaO + H_2O$) and the thermal decomposition of calcium carbonate ($CaCO_3 \rightarrow CaO + CO_2$), respectively, indicate the presence of 3.43 wt% portlandite and 3.97 wt% calcium carbonate due to an incomplete reaction.

TEM analysis of the sample collected at 35′ showed multiple non-oriented aggregates of rod-like hemihydrate nanocrystals 25–50 nm in length and 15–20 nm thick, along with larger shapeless or globular amorphous particles (*i.e.*, unreacted Ca-ethoxide and $Ca(OH)_2$) (Fig. 2a). After 45′ the shapeless and amorphous globular particles were no longer detected,

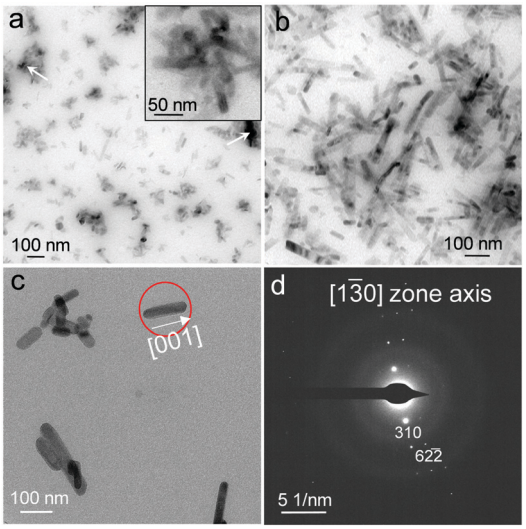

Fig. 2 TEM-SAED analysis of nanobassanite: (a) aggregates of bassanite nanorods (<200 nm in size) obtained after 35′, along with larger (300–500 nm) shapeless particles corresponding to aggregates of precursor Ca-ethoxide and portlandite (white arrows). The inset shows a detail of aggregated bassanite nanorods; (b) bassanite nanorods after 45′ reaction time; (c) bassanite nanorods after 55′. The orientation of the *c*-axis of the red-circled nanorod is indicated (based on SAED results shown in (d)); (d) SAED pattern of the red-circled nanorod in (c). Indexing have been performed considering the structure (*I*2 space group) of ref. 23.

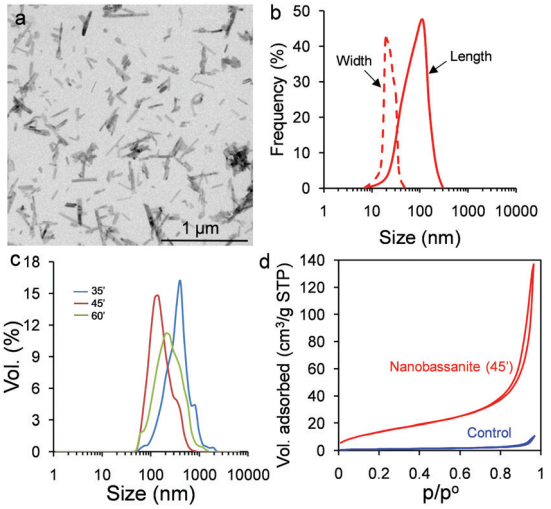

Fig. 3 PSD and N_2 sorption isotherms of bassanite nanorods: (a) representative TEM image of bassanite nanorods formed after 45′ reaction time; (b) PSD of the particles in (a) determined by direct measurement of the length (continuous line) and width (dashed line) of individual crystals; (c) DLS-derived PSD curves for nanobassanite synthesized at 35′, 45′ and 60′ reaction time; (d) sorption isotherms of nanobassanite synthesized at 45′ reaction time (red curves) as compared to standard (control) β-hemihydrate (blue curves).

indicating the full consumption of precursors. In parallel, abundant hemihydrate nanorods, which preferentially grew along the *c* axis, were observed (Fig. 2b and c). Crystal length increased with reaction time from ~120 nm at 45′ up to ~500 nm at 60′, while thickness did not vary significantly. Fig. 2d shows the SAED pattern of the rod-like nanoparticles with features of the reciprocal lattice and *d*-spacings corresponding to bassanite with space group *I*2.[23] Analysis of particle size distribution (PSD) using TEM images showed a narrow Log-normal distribution, as exemplified for the 45′ run where particles have mean length of 120 nm and width of 22 nm (Fig. 3a and b). TEM observations are in good agreement with dynamic light scattering (DLS) analysis (Fig. 3c), showing average particle size of 135 and 210 nm after 45′ and 60′ reaction time, respectively. After 35′, however, an average particle size of 330 nm is observed consistent with the presence of the larger aggregates of unreacted amorphous Ca-ethoxide and $Ca(OH)_2$ observed using TEM. At longer reaction times (≥45′) and complete precursor(s) transformation, bassanite nanorods were the only particles contributing to the PSD observed with DLS. The change in mean PSD between 45′ and 60′ reaction time is consistent with a coarsening mechanism (Ostwald ripening). These results show that a careful control of the reaction time is critical to achieve maximum conversion of precursors and minimum increase in crystal size.

N_2 sorption analysis (BET method) shows that the product obtained at 35′ had a SSA of 78 $m^2\ g^{-1}$. The actual contribution of the hemihydrate *vs.* the untransformed precursors to such a huge SSA is, however, unclear. The SSA of phase-pure bassanite collected after 45′ was 54.2 $m^2\ g^{-1}$, and decreased to 44 and 31 $m^2\ g^{-1}$ after 55′ and 60′, respectively, due to the observed coarsening. To our knowledge, 54.2 $m^2\ g^{-1}$ is the highest SSA value for pure hemihydrate reported so far. Nano-bassanite displays a Type II isotherm with H3 hysteresis (Fig. 3d), corresponding to non-microporous solids with interparticle (slit-shaped) meso- and macro-pores.[24] This is consistent with the features of hemihydrate nanorod aggregates observed with TEM (Fig. 2b).

The formation of phase-pure bassanite nanoparticles using this synthesis route can be rationalized considering that there is a large amount of ethanol in the synthesis medium, which reduces the system's water activity, hence increasing supersaturation with respect to any solid product.[17] A very high nucleation rate[14] and limited growth of metastable lower hydrates will thus be favored.[1,15,17] The fact that anhydrite forms in the absence of toluene shows that this solvent, which speeds Ca–alkoxide hydrolysis[20] but does not contribute to a reduction in water activity, is crucial to balance these two critical parameters, fostering nanobassanite formation.

Considering that a main application of bassanite involves its conversion to gypsum *via* hydration (*e.g.*, used as a cementing agent in construction or biomaterial applications), we evaluated its hydration kinetics, as compared with those of standard β-hemihydrate (plaster of Paris), with SSA of 3.72 $m^2\ g^{-1}$ and particle size of 1–2 μm (details in ESI†). Note that such SSA and particle size values are standard for commercial α- and β-hemihydrate.[19] Solids were subjected to (details in ESI†): (i) through-solution liquid-phase (LP) hydration (relevant for the reactivity – dissolution and setting – of nanobassanite used as a drug carrier and in orthopedics applications);[4–6] and (ii) vapor-phase (VP) hydration (relevant for alcohol dispersions of nanobassanite, similar to nanolimes,[25] to be used as a potential consolidant for historic gypsum plaster).

Fig. 4a and b show the evolution of the fractional conversion of (nano)bassanite into gypsum during LP and VP hydration, respectively. Fig. 4c and d show the good fitting

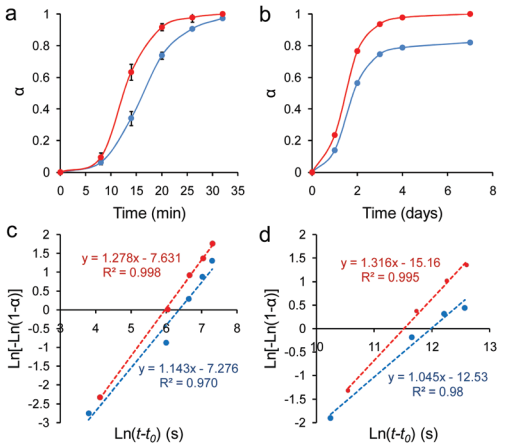

Fig. 4 Hydration kinetics. Time evolution of the fractional conversion (α) of nanobassanite (red circles/curves) and control (Plaster of Paris, β-hemihydrate; blue circles/curves) into gypsum following through-solution (a) and vapor phase (b) hydration. Error bars show standard deviation. Sharp-Hannock plots for the LP (c) and VP (d) hydration of (nano)bassanite. The red and blue circles are experimental points for nanobassanite and β-hemihydrate, respectively. The dashed lines are best linear fits to such experimental points using the Avrami-Erofe'ev equation (fitting parameters and R^2 values are indicated).

($R^2 \geq 0.97$) of these results to the Avrami model.[26] From this kinetics analysis (see Methods in ESI†) apparent rate constants (k) were calculated yielding: (LP) $k_{Control} = 1.72 \times 10^{-3}$ s^{-1} ($n = 1.14$) and $k_{Nanobass} = 2.56 \times 10^{-3}$ s^{-1} ($n = 1.27$) (Fig. 4c); (VP) $k_{Control} = 6.21 \times 10^{-6}$ s^{-1} ($n = 1.05$) and $k_{Nanobass} = 9.96 \times 10^{-6}$ s^{-1} ($n = 1.32$) (Fig. 4d). These results demonstrate that the hydration of the synthesized nanobassanite proceeds at a significantly faster rate (with a significantly higher conversion in the case of VP hydration; see Fig. 4b) than the low-SSA control (standard β-hemihydrate).

In summary, herein we report a novel route for the synthesis of high SSA, rod-shaped bassanite nanoparticles following a one-pot, solvothermal route that involves the formation of amorphous Ca-ethoxide and its transformation into nanobassanite after acid–base neutralization using concentrated sulfuric acid. The hydration kinetics study confirmed the exceptionally high reactivity of the synthesized nanomaterial as compared to a commercial control. This synthesized product is of special interest for applications in heritage conservation and for biomedical and pharmaceutical purposes.[4–6] In particular, by analogy to nanolimes having wide-ranging applications in heritage conservation,[25] the synthesized nanobassanite can be dispersed in ethanol (*e.g.*, 5–10 g L^{-1}) and applied (*e.g.*, by brushing or spraying) as consolidant to decayed porous gypsum-based substrates where the nanoparticles can penetrate in depth and, following solvent evaporation and VP hydration, can produce new gypsum cement. This treatment shows great potential in the heritage conservation field, responding to the urgent need of compatible consolidants for degraded historic gypsum plasters. Currently we are testing the application of alcohol dispersion of nanobassanite (*i.e.*, what we call "Nanogypsum") for the consolidation of Islamic period (middle age) gypsum plasters at the Alhambra (Granada, Spain).

We acknowledge financial support by the Spanish Government (grant RTI2018-099565-B-I00), Junta de Andalucía (Research Group RNM-179) and University of Granada, UGR (Research Excellence Unit UCE-PP2016-05 "Carbonates"). We also thank the personnel of the Centro de Instrumentación Científica, UGR, for their help during TEM and TG/DSC analyses. MBR acknowledges a doctoral research contract funded by the Spanish Government (PRE2019-090256).

Conflicts of interest

There are no conflicts to declare.

References

1 (*a*) T. M. Stawski, A. E. S. Van Driessche, M. Ossorio, J. D. Rodriguez-Blanco, R. Besselink and L. G. Benning, *Nat. Commun.*, 2016, **7**, 11177; (*b*) A. E. S. Van Driessche, T. M. Stawski and M. Kellermeier, *Chem. Geol.*, 2019, **530**, 119274.
2 B. Tian and M. D. Cohen, *Cem. Concr. Res.*, 2000, **30**, 117–123.
3 K. Elert, C. Benavides-Reyes and C. Cardell, *Cem. Concr. Compos.*, 2019, **96**, 274–283.
4 (*a*) M. A. Rauchsmann, T. A. Wichelhaus, V. Stirnal, E. Dingeldein, L. Zichner, R. Schnettler and V. Alt, *Biomaterials*, 2005, **26**, 2677–2684; (*b*) M. Sidqui, P. Collin, C. Vitte and N. Forest, *Biomaterials*, 1995, **16**, 1327–1332.
5 R. Butta, C. R. Tredwin, M. Nesbit and D. R. Moles, *J. Prosthet. Dent.*, 2005, **93**, 540–544.
6 Y. Jiang, H. Qin, H. Wan, J. Yang, Q. Yu, M. Jiang and B. Yu, *J. Cell. Mol. Med.*, 2020, **00**, 1–13.
7 D. Freyer and W. Voight, *Monatsh. Chem.*, 2003, **134**, 693–719.
8 N. B. Singh and B. Middendorf, *Prog. Cryst. Growth Charact. Mater.*, 2007, **53**, 57–77.
9 (*a*) H. J. Engert and T. Kolowski, *ZKG Int.*, 1998, **51**, 229–237; (*b*) B. Guan, G. Jiang, Z. Wu, J. Mao and B. Kong, *J. Am. Ceram. Soc.*, 2011, **94**, 3261–3266.
10 H. Fu, B. Guan and Z. Wu, *Fuel*, 2015, **150**, 602–608.
11 L. Li, Y. J. Zhu and M. G. Ma, *Mater. Lett.*, 2008, **62**, 4552–4554.
12 S. K. Lee, M. K. Lee and H. Lee, *J. Electrochem. Soc.*, 2010, **157**, K43–K46.
13 (*a*) B. Guan, G. Jiang, H. Fu, L. Yang and Z. Wu, *Ind. Eng. Chem. Res.*, 2011, **50**, 13561–13567; (*b*) B. Kong, B. Guan, M. Z. Yates and Z. Wu, *Langmuir*, 2012, **28**, 14137–14142; (*c*) Q. Chen, G. Jiang, C. Jia, H. Wang and B. Guan, *CrystEngComm*, 2015, **17**, 8549–8554; (*d*) P. Tartaj, J. Morales and L. Fernandez-Diaz, *Cryst. Growth Des.*, 2015, **15**, 2809–2816; (*e*) S. Fukugaichi and N. Matsue, *ACS Omega*, 2018, **3**, 2820–2824; (*f*) C. Hazra, S. Bari, D. Kundu, A. Chaudhari, S. Mishra and A. Chatterjee, *Ultrason. Sonochem.*, 2014, **21**, 1117–1131.
14 Y. W. Wang, Y. Y. Kim, H. K. Christenson and F. C. Meldrum, *Chem. Commun.*, 2012, **48**, 504–506.
15 U. Tritschler, A. E. S. Van Driessche, A. Kempter, M. Kellermeier and H. Cölfen, *Angew. Chem., Int. Ed.*, 2015, **54**, 4083–4086.
16 Y. W. Wang and F. C. Meldrum, *J. Mater. Chem.*, 2012, **22**, 22055–22062.
17 U. Tritschler, M. Kellermeier, C. Debus, A. Kempter and H. Cölfen, *CrystEngComm*, 2015, **17**, 3772.
18 Q. Chen, C. Jia, Y. Li, J. Xu, B. Guan and M. Z. Yates, *Langmuir*, 2017, **33**, 2362–2369.
19 Y. B. Park, K. Mohan, A. Al-Sanousi, B. Almaghrabi, R. J. Genco, M. T. Swihart and R. Dziak, *Biomed. Mater.*, 2011, **6**, 055007.
20 K. T. Ranjit and K. J. Klabunde, *Chem. Mater.*, 2005, **17**, 65–73.
21 J. Bensted and S. Prakash, *Nature*, 1968, **219**, 60–61.
22 D. A. Powell, *Nature*, 1958, **182**, 792.
23 C. Bezou, A. Nonat, J.-C. Mutin, A. N. Christensen and M. S. Lehmann, *J. Solid State Chem.*, 1995, **117**, 165–176.
24 K. S. W. Sing, D. H. Everett, R. A. W. Haul, L. Moscou, R. A. Pierotti, J. Rouquerol and T. Siemieniewska, *Pure Appl. Chem.*, 1985, **57**, 603–619.
25 C. Rodriguez-Navarro and E. Ruiz-Agudo, *Pure Appl. Chem.*, 2018, **90**, 523–550.
26 S. J. Gurgul, G. Seng and G. R. Williams, *J. Synchrotron Radiat.*, 2019, **26**, 774–784.